

## Article

# Rechargeable Magnesium Ion Batteries Based on Nanostructured Tungsten Disulfide Cathodes

Wuqi Guo, Dorian A. H. Hanaor \*, Delf Kober, Jun Wang, Maged F. Bekheet \* and Aleksander Gurlo

Chair of Advanced Ceramic Materials, Institute of Material Science and Technology, Faculty III Process Sciences, Technische Universität Berlin, Straße des 17. Juni 135, 10623 Berlin, Germany

\* Correspondence: dorian.hanaor@ceramics.tu-berlin.de (D.A.H.H.); maged.bekheet@ceramics.tu-berlin.de (M.F.B.)

**Abstract:** Finding effective cathode materials is currently one of the key barriers to the development of magnesium batteries, which offer enticing prospects of larger capacities alongside improved safety relative to Li-ion batteries. Here, we report the hydrothermal synthesis of several types of  $\text{WS}_2$  nanostructures and their performance as magnesium battery cathodes. The morphology of  $\text{WS}_2$  materials was controlled through the use of sodium oxalate as a complexing agent and different templating agents, including polyethylene glycol (PEG), polyvinylpyrrolidone (PVP), and hexadecyltrimethyl ammonium bromide (CTAB). A high capacity of 142.7 mAh/g was achieved after 100 cycles at a high current density of 500 mA/g for cathodes based on a nanostructured flower-like  $\text{WS}_2$ . A solution consisting of magnesium (II) bis(trifluoromethanesulfonyl)imide ( $\text{MgTFSI}_2$ ) and magnesium (II) chloride ( $\text{MgCl}_2$ ) in dimethoxyethane (DME) was used as an effective electrolyte, which contributes to favorable  $\text{Mg}^{2+}$  mobility. Weaker ionic bonds and van der Waals forces of  $\text{WS}_2$  compared with other transition metal oxides/sulfides lay the foundation for fast discharge/charge rate. The enhanced surface area of the nanostructured materials plays a key role in enhancing both the capacity and discharge/charge rate.

**Keywords:** magnesium-ion batteries; tungsten sulfide; XRD; impedance spectroscopy; hydrothermal synthesis



**Citation:** Guo, W.; Hanaor, D.A.H.; Kober, D.; Wang, J.; Bekheet, M.F.; Gurlo, A. Rechargeable Magnesium Ion Batteries Based on Nanostructured Tungsten Disulfide Cathodes. *Batteries* **2022**, *8*, 116. <https://doi.org/10.3390/batteries8090116>

Academic Editors: Pascal Venet, Karim Zaghib and Seung-Wan Song

Received: 28 July 2022

Accepted: 30 August 2022

Published: 6 September 2022

**Publisher's Note:** MDPI stays neutral with regard to jurisdictional claims in published maps and institutional affiliations.



**Copyright:** © 2022 by the authors. Licensee MDPI, Basel, Switzerland. This article is an open access article distributed under the terms and conditions of the Creative Commons Attribution (CC BY) license (<https://creativecommons.org/licenses/by/4.0/>).

## 1. Introduction

Lithium-ion batteries have emerged as the most prominent electrochemical energy storage systems over the past two decades, and much progress has been achieved in the design of lithium-ion battery materials and systems [1–4]. In recent years, magnesium-ion batteries have been the subject of intensive research towards so-called post lithium batteries, particularly for applications in electric vehicles [5]. In contrast to lithium, which sources are of limited geological availability, magnesium has a high abundance in Earth's crust (approximately 1.5 wt%). When compared with lithium-ion batteries, magnesium-ion systems possess numerous advantages, including a high theoretical volumetric energy density of 3833 mAh/mL (vs. 2046 mAh/mL for Li-metal anode) and a high gravimetric capacity of 2205 mAh/g, alongside a lower tendency for anodic dendrite formation, which alleviates one of the key safety concerns associated with Li-ion batteries [6]. Additionally, compared with other anode candidates, metallic magnesium has a strongly negative reduction potential of  $-2.3$  V versus a standard hydrogen electrode [7]. Despite these advantages, there remain significant obstacles to the future implementation of magnesium-based batteries [8]. The first challenge is that the solvent of traditional electrolytes used in lithium-ion batteries tends to react with magnesium anodes to form a dense passivating layer, blocking both electron and cation transport, thus limiting potential cathode/electrolyte material combinations. Further hurdles lie in low ion mobility and poor performance of existing cathode candidates. Metal oxides, including  $\text{V}_2\text{O}_5$  and  $\text{TiO}_2$ , have commonly been adopted as experimental

cathodes in magnesium batteries as these materials are expected to exhibit high energy capacity and stability [9]. However, divalent magnesium ions experience significant electrostatic barriers at interfaces in such metal oxide cathodes, leading to sluggish solid-state diffusion of magnesium ions and slow interfacial charge transfer [10]. Ion mobility is further impeded in some commonly used electrolytes such as tetrahydrofuran (THF) solution of organomagnesium chloroaluminate complex  $Mg(AlCl_2BuEt)_2$ , where Bu and Et are butyl and ethyl groups, respectively, (denoted as DCC) and THF/phenylmagnesiumchloride ( $PhMgCl$ )/ $AlCl_3$  (all phenyl complex electrolyte, denoted as APC) that consist of large molecules [5,11]. In order to increase electrochemical performance in battery tests, various alternative cathode materials have been investigated in the past several years, notably metal sulfides. Chevrel phase  $Mo_6S_8$  was the first identified cathode material for magnesium batteries that exhibited relatively good reversibility, charging kinetics, and life-span [12]. However, this cathode material and its analogs bring about rather low operating voltages and energy densities [13]. Relative to oxides, transition metal (TM) chalcogenides, such as  $TiS_2$ ,  $MoS_2$ , and  $TiSe_2$ , offer the scope for improved cathode performance due to their electrostatic interactions with  $Mg^{2+}$  ions [8–10]. For TM chalcogenides, metals and sulfur atoms firstly bond covalently to form the two-dimensional S-TM-S tri-layers, which leads to a sandwich structure through weak van der Waals forces between layers. This structure allows the production of nanostructured materials such as nanosheets, nanotubes, and fullerene-like nanoparticles, which provide space for ion intercalation, thus enabling faster kinetics and better cycling and rate performance. Recently, promising results have been reported for cathodes based on TM chalcogenides [14–22]. Compared with transition metal oxides, they exhibit relatively good compatibility with electrolytes and have shown higher operating voltage, energy density, and stability compared with Chevrel phases [5,10]. In the presently reported study, novel nano  $WS_2$  cathodes with different morphologies are investigated as cathodes in Mg-ion batteries [23]. Tungsten disulfide was chosen for this work because both ionic bonds and van der Waals forces in  $WS_2$  are weaker in comparison with other TM chalcogenides, which should enhance ion mobility, with implications for performance as magnesium battery cathodes [24]. Moreover, due to weaker bonding forces,  $WS_2$  can readily be produced with various nanostructured morphologies [25].  $WS_2$  is considered a desirable intercalation host material for magnesium batteries as guest ions are expected to intercalate in the lattice host reversibly and diffuse quickly through its looser stacked layers [26]. Here, we target the fabrication of magnesium batteries based on  $WS_2$  cathodes with high ion mobility and good capacity/reversibility. Sodium oxalate,  $Na_2C_2O_4$ , is used as a complexing agent, and different organic templates are added to modify the morphology of the obtained  $WS_2$  nanostructures. We further compared two electrolyte candidates based on dimethoxyethane (DME)/magnesium (II) bis(trifluoromethanesulfonyl)imide ( $MgTFSI_2$ )/magnesium (II) chloride ( $MgCl_2$ ) (referred to here as DMM) and APC electrolyte for use with the investigated cathode materials. APC electrolyte is a commonly used magnesium battery electrolyte, while DME is a better ethereal solvent than the THF used in APC owing to faster ion mobility and reduced toxicity [5,11].  $MgCl_2$  was used to stabilize the DMM electrolyte and dissolve the passivation film formed during battery cycling [11]. Compared with more commonly used Mg battery electrolytes, such as APC, this electrolyte provides a broader electrochemical window, reduced corrosion of current collectors due to a lower  $MgCl_2$  content, higher Mg ion mobility, and better reversibility and cycling performance [5].

We report here an experimental study conducted to examine whether  $WS_2$  serves to impart favorable battery performance in terms of ion mobility and examine the role of different cathode morphology and electrolyte compositions (APC and DMM) on overall electrochemical performance. We produced nanostructured  $WS_2$  with different morphologies by means of a hydrothermal method and applied these materials as cathodes in magnesium-ion batteries. The morphologies were formed by adding  $Na_2C_2O_4$  as a complexing agent and polyethylene glycol (PEG), polyvinylpyrrolidone (PVP), or hexadecyltrimethyl ammonium bromide (CTAB) as templates. APC and DMM electrolytes were adopted as electrolytes

in this research. WS<sub>2</sub> samples were named as follows: WS<sub>2</sub>-bulk (without the use of additives), WS<sub>2</sub>-OX (with sodium oxalate complexing agent), WS<sub>2</sub>-OX-PEG (sodium oxalate and PEG), WS<sub>2</sub>-OX-PVP (sodium oxalate and PVP), and WS<sub>2</sub>-OX-CTAB (sodium oxalate and CTAB), respectively.

## 2. Materials and Methods

*Reagents and materials:* All reagents were purchased from Sigma-Aldrich with a purity of >99.9%. Nickel (99.9%) and magnesium (99.9%) foil were acquired from Goodfellow. MgTFSI<sub>2</sub>, MgCl<sub>2</sub>, and AlCl<sub>3</sub> were dried under vacuum at 120 °C prior to synthesis.

*Hydrothermal synthesis of WS<sub>2</sub> powders:* In a typical synthesis, 1.50 g sodium tungstate dihydrate, Na<sub>2</sub>WO<sub>4</sub>·2H<sub>2</sub>O, 1.50 g thioacetamide, C<sub>2</sub>H<sub>5</sub>NS and 2.00 g of sodium oxalate, Na<sub>2</sub>C<sub>2</sub>O<sub>4</sub> were dissolved in 25 mL deionized water by vigorous stirring for 5 min. Subsequently, 0.50 g quantities of PEG, PVP, and CTAB were added as organic templating surfactants to the solution under vigorous stirring with continued ultrasonication for 10 min. The obtained clear solution was adjusted to pH 1 by HCl, sealed in a 50 mL stainless steel autoclave (Teflon-lined), and kept heating at 220 °C for 20 h. The autoclave was opened after cooling to room temperature, and the dark grey precipitate was collected and purified by repeated centrifugation with ethanol and water. The product was vacuum dried at 80 °C overnight and annealed at 950 °C in an argon atmosphere overnight.

*Preparation of electrolyte:* The APC electrolyte solution was synthesized in a glove box under argon following the procedure described in reference [11]. First, 1.34 g AlCl<sub>3</sub> was added slowly to 15 mL THF solvent under vigorous stirring to obtain the targeted concentration. Subsequently, the acquired solution was dropwise added to a 10 mL PhMgCl/THF solution (2 M PhMgCl), followed by stirring for 16 h at room temperature. The process of electrolyte preparation is exothermic.

MgTFSI<sub>2</sub> is the only ether-soluble magnesium salt and was therefore selected for this work. The practicality of MgTFSI<sub>2</sub> solution as a viable electrolyte for Mg batteries is hindered by the poor electrochemical performance of Mg anodes in MgTFSI<sub>2</sub> solutions. MgTFSI<sub>2</sub>/DME solutions, on the other hand, have been shown to dissolve a large amount of MgCl<sub>2</sub> and produce electrolyte solutions with good performance. The DMM electrolyte was prepared in a glove box following the process detailed in reference [27]. In this synthesis, 1.46 g MgTFSI<sub>2</sub> and 0.12 g anhydrous MgCl<sub>2</sub> were added to 10 mL DME followed by stirring for 6 h at 70 °C and filtering.

Before battery testing, the electrolyte was processed by galvanostatic conditioning (CHI600E Potentiostat, CH Instruments Inc., Shanghai, China), involving a repeated passage of constant current while following the over-potential of the cathodic process (Mg deposition). In the initial stage, a high over-potential for deposition of 0.8 V for the first few cycles was exhibited in fresh MgTFSI<sub>2</sub>/MgCl<sub>2</sub> solution. During cycling, the over-potential of Mg deposition stabilized at a low value of less than 0.2 V after decreasing from cycle to cycle, indicating an optimal composition was reached for the solution. The behavior of the DME/MgTFSI<sub>2</sub>/MgCl<sub>2</sub> solutions used as the DMM electrolyte is reflected by cyclic voltammetry (CV) data, which reveals a wide electrochemical window of >3.1 V, over 99% Mg deposition/dissolution efficiency, and a low Mg deposition over-potential of less than 0.2 V.

*Characterization:* X-ray diffraction (XRD) patterns were collected from specimen powders in a Bruker AXS D8 ADVANCE X-ray diffractometer (Bruker, Billerica, MA, USA) with Co K $\alpha$  radiation ( $\lambda = 0.1789$  nm). The measurements were conducted between 10° and 90° 2θ value (step size-0.02; 8 s per step).

A scanning electron microscopy (SEM, LEO 1530, Zeiss, Jena, Germany) was used to analyze the microstructure of synthesized powders. The samples were prepared by putting a small amount of powder on the adhesive carbon tape. An accelerating voltage of 5 kV was used for collecting images.

X-ray photoelectron spectroscopy (XPS) measurements were conducted on an ESCALAB 250Xi instrument (Thermo Fisher Scientific, Waltham, MA, USA). The X-ray spot

size was 100  $\mu\text{m}$ . Powders were sprinkled on the carbon conductive tape in the glove box for the preparation of samples. The C 1s core line with a binding energy of 284.8 eV was used for calibration of all XPS spectra. The data were processed by using XPS Peak41 software. The Lorentzian–Gaussian ratios in peak fitting have been constrained between 20 and 30. Shirley backgrounds were used in all fittings.

A QuadraSorb Station 4 instrument (Quantachrome, Boynton Beach, FL, USA) was used for the nitrogen sorption tests in this research. After degassing under a vacuum at 150 °C for 12 h, we recorded isotherms at 77 K before the measurement. Brunauer–Emmett–Teller (BET) calculations were used for the calculation of the surface area. The Quantachrome/QuadraWin software version 5.05 was used to analyze all nitrogen sorption data.

*Preparation of coin cells:* All the following procedures were conducted in a glove box under an inert atmosphere with H<sub>2</sub>O and O<sub>2</sub> less than 0.1 ppm. Coin cell cases (CR2032 type), spacers, springs, and o-rings produced by Mitsubishi® were used. A slurry of 75 wt.% active material, 10 wt.% Super-P carbon back and 15 wt.% polyvinylidene fluoride dispersed in N-methyl-2-pyrrolidone (NMP) were prepared by wet grinding for 1 h. For the working electrode (cathode) fabrication, this slurry was then tape-cast on nickel foil and dried, first in the air at 50 °C and then under vacuum at 100 °C. The resulting mass loading of the active cathode material was 1.2 mg/cm<sup>2</sup>. The coated working electrodes were then pressed at a pressure of 80–120 kg/cm<sup>2</sup> and were cut into circular forms of 16 mm in diameter. Magnesium foil, having the same diameter with a thickness of 0.25 mm, was adopted as the anode material. Whatman® glass fiber filter paper (GF/A) was adopted as a separator.

*Coin cell testing:* Battery testing was conducted using a CT2001A battery tester system (Wuhan LAND, Wuhan, China). Galvanostatic discharge–charge measurements were conducted in the potential range of 0.05–2 V versus Mg<sup>2+</sup>/Mg at 500 mA/g. Data points were collected every 3 s. Cyclic voltammetry (CV) was carried out on a CHI660B electrochemical workstation with a 1 mV/s scanning rate in the potential window of 0–2 V. WS<sub>2</sub>-OX-PVP and DMM are used as cathode and electrolyte in the CV measurement. Pulsed discharge/charge tests and electrochemical impedance spectroscopy (EIS) measurements were conducted on coin cells with the selected WS<sub>2</sub>-bulk and WS<sub>2</sub>-OX-PVP electrodes with DMM electrolyte and WS<sub>2</sub>-OX-PVP electrodes with APC electrolyte. A Zahner Im6ex workstation (Zahner, Kronach, Germany) was used for the measurement conduction in potentiostatic mode with 5 mV amplitude between 50 mHz and 1 MHz. The tested cell was firstly discharged to 5 mV and then charged to 2.0 V at 75 mA/g. The tested cells were discharged and charged with pausing intervals at certain cell potentials (0.3, 0.6, 1.0, and 2.0 V) and were rested for two hours prior to EIS measurement.

### 3. Results and Discussion

XRD patterns of synthesized WS<sub>2</sub> materials (Figure 1a) are well matched with the calculated reference pattern of the reported structure of WS<sub>2</sub> (JCPDS No. 08-0237) [28–31], indicating that the obtained products crystallize in a hexagonal crystal structure with space group *P*6<sub>3</sub>/*mmc* (No. 194). No diffraction peaks of any impurity phases were observed in the XRD patterns, and all peaks are well defined, indicative of a well-crystallized single phase after heat treatment. Anisotropic broadening in XRD reflections was observed to varying extents in XRD patterns of all samples, suggesting an anisotropic crystallite size in the synthesized WS<sub>2</sub> phase. This anisotropic crystal growth is consistent with the formation of 2D-like structures of WS<sub>2</sub>, in which the (002) reflection indicates the number of stacked WS<sub>2</sub> layers along the *c*-axis. Similar to graphite, the average number *N<sub>c</sub>* of WS<sub>2</sub> stacking layers can be estimated from interplanar spacing *d*<sub>002</sub> and crystallite size along the *c*-axis (*L<sub>c</sub>*) [32,33]. To gain further insights into lattice parameters, crystallite size, and width of stacking layer in the samples, a Le Bail whole-profile fitting method [34] was applied to diffraction patterns using FULLPROF software [35] with the profile function 7 (Thompson–Cox–Hastings pseudo-Voigt convoluted with axial divergence asymmetry function) [36]. The resolution function of the diffractometers was obtained from the structure refinement

of a LaB<sub>6</sub> standard. Figures 1a and S1 show the observed, calculated, and difference for the final cycle of the profile fitting of the whole XRD pattern for WS<sub>2</sub>-bulk. As shown in Figure S1, the XRD pattern fitting using a sphere model with isotropic peak broadening for all XRD reflections in initial refinement attempts yielded poor fitting (convergence factors  $R_{wp} = 18.5\%$  and  $X^2 = 9.3$ ). In contrast, the use of an anisotropic broadening model (Isizemodel = 6, in which the broadening is considered only for reflections of the form: (h0l)) for crystallite size resulted in better fitting with good convergence factors  $R_{wp} = 9.3\%$  and  $X^2 = 2.1$  (Figure S1). Similarly, the XRD patterns of other samples are better fitted with the anisotropic size broadening model rather than the isotropic model. These results confirm the formation of 2D WS<sub>2</sub> materials in all samples. The lattice parameter, unit cell volume, interplanar spacing  $d_{002}$ , crystallite size, and the average number  $N_c$  of WS<sub>2</sub> stacking layers determined from XRD analysis are listed in Table S1. As shown in Table S1, all samples show very close values of lattice parameters, which are in good agreement with previously reported values [28–31]. These results confirm the formation of stoichiometric pristine WS<sub>2</sub> containing tetravalent W<sup>4+</sup> cations under the present experimental conditions. The XRD pattern of WS<sub>2</sub>-bulk shows the sharpest (002) reflections because it has the largest crystallite size and the highest number of stacking layers along the *c* direction. In contrast, the WS<sub>2</sub>-OX sample has the smallest  $L_c$  and lowest  $N_c$ ; thus, it exhibits the broadest (002) reflections.

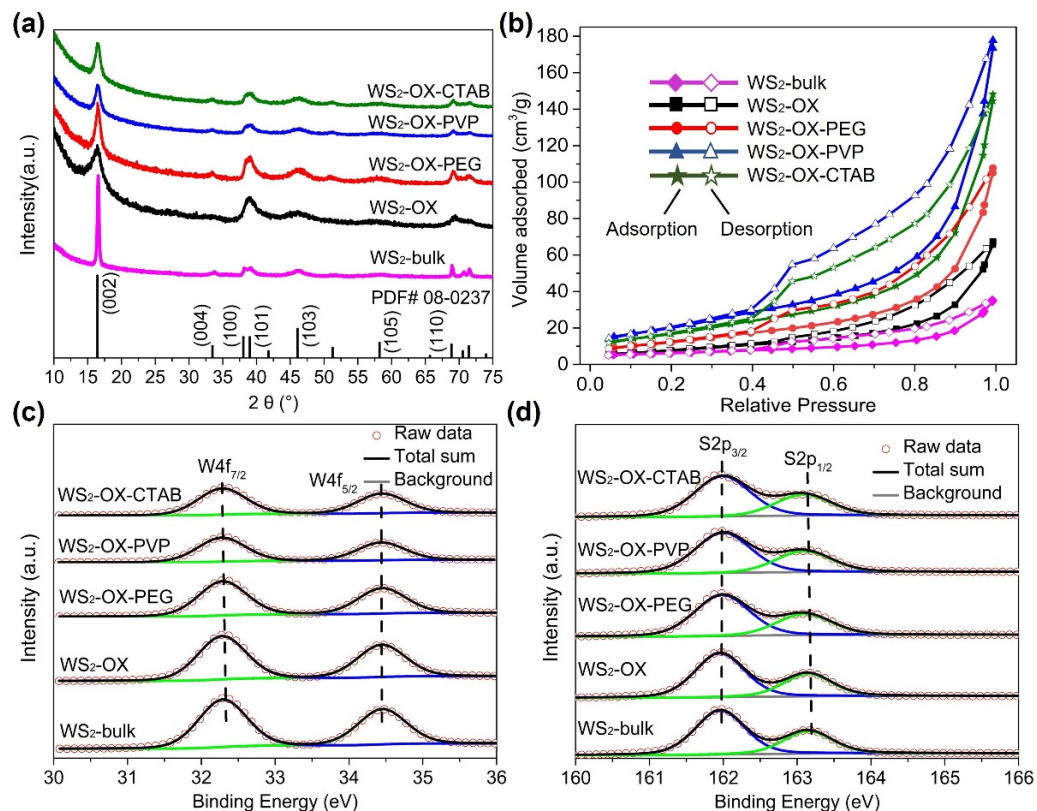


**Figure 1.** (a) XRD patterns of WS<sub>2</sub>-bulk, WS<sub>2</sub>-OX, WS<sub>2</sub>-OX-PEG, WS<sub>2</sub>-OX-PVP, and WS<sub>2</sub>-OX-CTAB. The calculated pattern of WS<sub>2</sub> reference (JCPDS No. 08-0237) is shown at the bottom. (b) Nitrogen sorption isotherms BET of WS<sub>2</sub>-bulk, WS<sub>2</sub>-OX, WS<sub>2</sub>-OX-PEG, WS<sub>2</sub>-OX-PVP, and WS<sub>2</sub>-OX-CTAB. (c,d) High-resolution X-ray photoelectron spectra of W4f and S2p for WS<sub>2</sub>-bulk, WS<sub>2</sub>-OX, WS<sub>2</sub>-OX-PEG, WS<sub>2</sub>-OX-PVP, and WS<sub>2</sub>-OX-CTAB.

In Figure 1b, BET analysis of the different WS<sub>2</sub> materials reveals curves exhibiting reversible type IV isotherms, which is one of the main characteristics of mesoporous materials. Based on the measured absorbed volume of each sample, WS<sub>2</sub> materials with ordered nanostructures (WS<sub>2</sub>-OX-PEG, WS<sub>2</sub>-OX-PVP, and WS<sub>2</sub>-OX-CTAB) have larger specific surface areas than that with disordered structure. WS<sub>2</sub> with nanoflower-sphere-

morphologies ( $\text{WS}_2\text{-OX-PVP}$  and  $\text{WS}_2\text{-OX-CTAB}$ ) show the largest specific surface area of 80 and 70  $\text{m}^2/\text{g}$ , respectively, while randomly stacked  $\text{WS}_2$  nanosheets in the  $\text{WS}_2\text{-OX}$  sample present a lower specific surface area of 28  $\text{m}^2/\text{g}$  and the  $\text{WS}_2\text{-bulk}$  sample possesses the lowest specific surface area of 10  $\text{m}^2/\text{g}$ .  $\text{WS}_2$  with nanorods morphology ( $\text{WS}_2\text{-OX-PEG}$ ) also shows an average surface of 57  $\text{m}^2/\text{g}$ . Usually, cathode materials with a high surface area are expected to provide more magnesium ion intercalation spots, in particular when the exposed plane and the kinetically probable diffusion axes are matching [9,11].

Figure 1c,d displays XPS of  $\text{WS}_2$  materials. The W 4f spectra of all samples are composed of a doublet peak at around 32.3 and 34.4 eV, corresponding to  $4\text{f}_{7/2}$  and  $4\text{f}_{5/2}$  transitions, respectively, implying the presence of  $\text{W}^{4+}$  ions in all samples. Similarly, the S2p spectra can be deconvoluted into a doublet at 163.2 and 161.9 eV, corresponding to the  $2\text{p}_{1/2}$  and  $2\text{p}_{3/2}$  transition. These values are in good agreement with previous reports for 2H- $\text{WS}_2$  [37] that report 32.3/34.4 eV for  $4\text{f}_{7/2}$  and  $4\text{f}_{5/2}$  and 161.9/163.2 eV for  $\text{S}2\text{p}_{1/2}$  and  $\text{S}2\text{p}_{3/2}$ , respectively. No shift in the binding energy is observed for any samples. In addition, the fitting of the W and S spectra revealed that the surface elemental composition was found to be 65.9 at% to 33.6 at% of W and S, respectively, in all samples, confirming the formation of stoichiometric  $\text{WS}_2$  containing tetravalent  $\text{W}^{4+}$  cations in all samples [38]. The XPS fitting results and parameters are summarized in Table S2.

Figure 2 shows SEM micrographs of materials prepared using different templating agents.  $\text{WS}_2\text{-bulk}$  clearly presents a well-ordered stacked microstructure, while the SEM image of  $\text{WS}_2\text{-OX}$  reveals a disordered morphology of randomly stacked nanosheets. The comparison of the two figures (Figure 2a,b) can serve to interpret the difference shown by XRD patterns of  $\text{WS}_2\text{-bulk}$  and  $\text{WS}_2\text{-OX}$  (Figures 1a and S1). Figure 2c–e present SEM images of  $\text{WS}_2\text{-OX-PEG}$ ,  $\text{WS}_2\text{-OX-PVP}$ , and  $\text{WS}_2\text{-OX-CTAB}$ , respectively. It can be seen that  $\text{WS}_2\text{-OX-PEG}$ ,  $\text{WS}_2\text{-OX-PVP}$ , and  $\text{WS}_2\text{-OX-CTAB}$ , respectively, present morphologies of nanorods, nanoflower-spheres, and nanoflower-aggregates. For  $\text{WS}_2\text{-OX-PEG}$ , the diameter of nanorods ranges from 100 nm to 200 nm, and the length is several micrometers.  $\text{WS}_2\text{-OX-PVP}$  and  $\text{WS}_2\text{-OX-CTAB}$  both exhibit flower-like forms consisting of numerous nanosheets with a thickness of several nanometers. The morphologies of  $\text{WS}_2\text{-OX-PVP}$  and  $\text{WS}_2\text{-OX-CTAB}$  differ in that the nanoflowers of  $\text{WS}_2\text{-OX-PVP}$  are present in the form of numerous submicron spheres while those of  $\text{WS}_2\text{-OX-CTAB}$  combine to form larger continuous nanoflower-aggregates. Additionally, the nanosheets formed in  $\text{WS}_2\text{-OX-PVP}$  are thinner and more uniform than those of  $\text{WS}_2\text{-OX-CTAB}$ . The morphology comparison results of  $\text{WS}_2\text{-OX}$ ,  $\text{WS}_2\text{-OX-PEG}$ ,  $\text{WS}_2\text{-OX-PVP}$ , and  $\text{WS}_2\text{-OX-CTAB}$  are consistent with the XRD analysis results above.

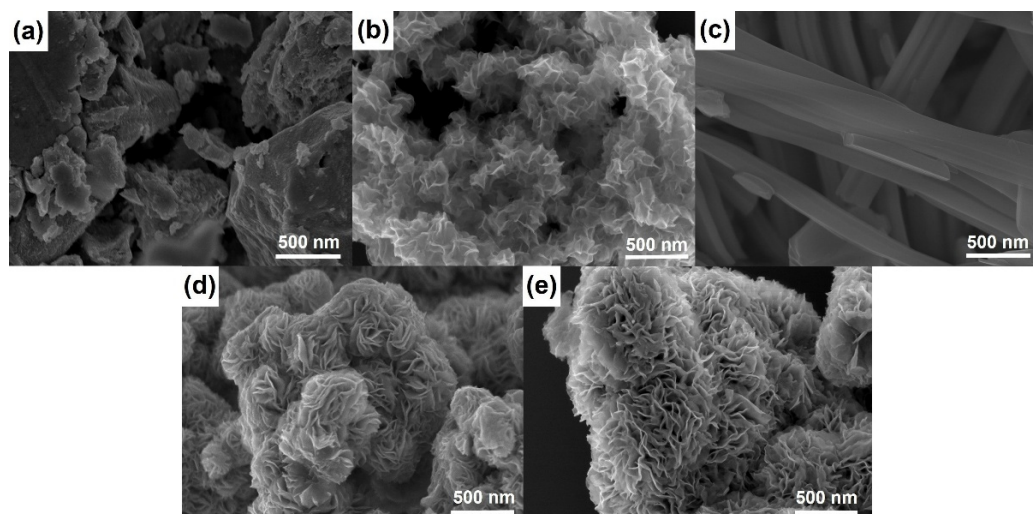


**Figure 2.** SEM images of  $\text{WS}_2\text{-bulk}$  (a),  $\text{WS}_2\text{-OX}$  (b),  $\text{WS}_2\text{-OX-PEG}$  (c),  $\text{WS}_2\text{-OX-PVP}$  (d), and  $\text{WS}_2\text{-OX-CTAB}$  (e) showing the different morphologies of  $\text{WS}_2$  in the samples after heat treatment.

The morphology of the electrode materials can influence the specific surface area and the available void space between the neighboring nanosheets, which is beneficial to the great improvement of electrochemical performance. To examine this conjecture, electrochemical tests were conducted.

Figure 3 shows the performance of WS<sub>2</sub> as cathodes in magnesium batteries at 500 mA/g in different electrolytes. In cells using an APC electrolyte, discharging capacities for all cathode types (WS<sub>2</sub>-bulk, WS<sub>2</sub>-OX, WS<sub>2</sub>-OX-PEG, WS<sub>2</sub>-OX-PVP, and WS<sub>2</sub>-OX-CTAB) declined sharply with the cycle number. Capacities achieved in the first full cycle are 10.4, 24.3, 98.5, 126.1, and 125.2 mAh/g, respectively (Table S3). For the final cycle, the capacities are 0.7, 3.5, 47.2, 64, and 55.1 mAh/g, respectively. In cells using DMM electrolytes, the discharge capacities showed a little decline over cycles. The trend indicates that coulombic efficiencies reached almost 100% showing very good reversibility. The highest capacities achieved for WS<sub>2</sub>-bulk, WS<sub>2</sub>-OX, WS<sub>2</sub>-OX-PEG, WS<sub>2</sub>-OX-PVP, and WS<sub>2</sub>-OX-CTAB are 6.4, 24.9, 133.5, 146.4, and 144.3 mAh/g, respectively (Table S3). These capacities remained stable over the first 100 cycles at a very high current density of 500 mA/g. For the final cycle, the capacities are 5.9, 23.7, 127.8, 142.7, and 137.6 mAh/g, respectively. It was observed that the battery performance was improved by using DMM instead of APC as the electrolyte. The retained charge capacities in cells using DMM electrolyte after 100 cycles are notably higher than those in APC cells after a few initial cycles. Moreover, the WS<sub>2</sub>-bulk and WS<sub>2</sub>-OX samples show very low specific capacity, indicating the electrochemical inactivity of these samples. These results might be explained by the small specific surface area of the WS<sub>2</sub>-bulk (10 m<sup>2</sup>/g) and WS<sub>2</sub>-OX (28 m<sup>2</sup>/g) samples. In contrast, the nanoflower morphology of WS<sub>2</sub>-OX-PVP and WS<sub>2</sub>-OX-CTAB samples resulted in a high specific area with 80 m<sup>2</sup>/g and 70 m<sup>2</sup>/g, respectively; thus, they show the best electrochemical performance. Although the WS<sub>2</sub>-OX-PEG sample shows a different morphology (i.e., nanorods), it still exhibits an average surface area of 57 m<sup>2</sup>/g and a reasonably good electrochemical performance. Although the WS<sub>2</sub>-OX sample exhibit similar morphology to that of WS<sub>2</sub>-OX-PVP and WS<sub>2</sub>-OX-CTAB, it shows a much lower electrochemical capacity than the latter two samples due to its low specific surface area (28 m<sup>2</sup>/g). Similar electrochemical inactivity was reported for MoS<sub>2</sub>/C cathodes due to the reduction in the specific surface area [19,23]. It is well known that a higher surface area of electrode materials in batteries could increase the contact area with the electrolyte, accessibility to the active sites, and utilization of the electrode capacity, often resulting in a higher specific capacity [39].

In order to understand the storage mechanism of Mg<sup>2+</sup> in the cathode materials and to estimate their theoretical capacities, cathodes were studied by XRD and SEM following discharge. Figure 4a,b show micrographs of the WS<sub>2</sub>-OX-PVP-based electrode in DMM electrolyte in charged and discharged states. No clear change in morphology is evident as a result of the discharging process. Similarly, Figure 4c, showing the XRD patterns for these samples, reveals that all the main XRD reflections remain after discharging, confirming the retention of the hexagonal structure of WS<sub>2</sub>. However, it is seen that the (002) reflection is shifted to notably lower 2θ angles after full discharge. The single fitting of this reflection reveals that it shifted from 2θ = 16.64°, corresponding to an interplanar d-spacing of 0.618 nm, before discharging to 2θ = 15.71°, corresponding to an interplanar d-spacing of 0.655 nm. In contrast, no remarkable shift is observed for the other reflections (e.g., (110) and (100)) after discharge. These results are consistent with the electrochemical intercalation of Mg<sup>2+</sup> ions between the WS<sub>2</sub> layers during the discharging process, leading to an increase in the interlayer distance  $d_{002}$  of the cathode host lattice. This implies that except for intercalation, no chemical modification occurs during the discharging process. Unlike several proposed Mg-S batteries [40], no new sulfide phases are formed here, nor do any exchange reactions take place during discharge, as is the case in conversion-type electrodes [41]. Figure S2 presents the schematic diagram of the magnesium intercalation process. The Mg<sup>2+</sup> intercalation/deintercalation process during discharging/charging could be substantiated by the cyclic voltammetry, which is shown in Figure 4d. As Figure 4d shows, the battery undergoes reversible Mg<sup>2+</sup> intercalation and deintercalation reactions,

which correspond to the reduction peak (around 0.5 V) and the oxidation peak (around 1.0 V). From Figure 3d, during the discharging–charging process, the discharging plateau appeared at around 0.5 V, and the charging plateau appeared at around 1.0 V. Therefore, the CV results are consistent with the discharging–charging profile shown in Figure 3d. The reduction peak at 0.5 V is related to the intercalation process (magnesiation), and the oxidation peak at 1.0 V is related to the deintercalation process (demagnesiation). Similar discharging–charging plateaus and the reduction–oxidation (intercalation–deintercalation) peaks could be found in the previous work with  $\text{WS}_2$  as a working electrode [42–44], which substantiates the results in this research.

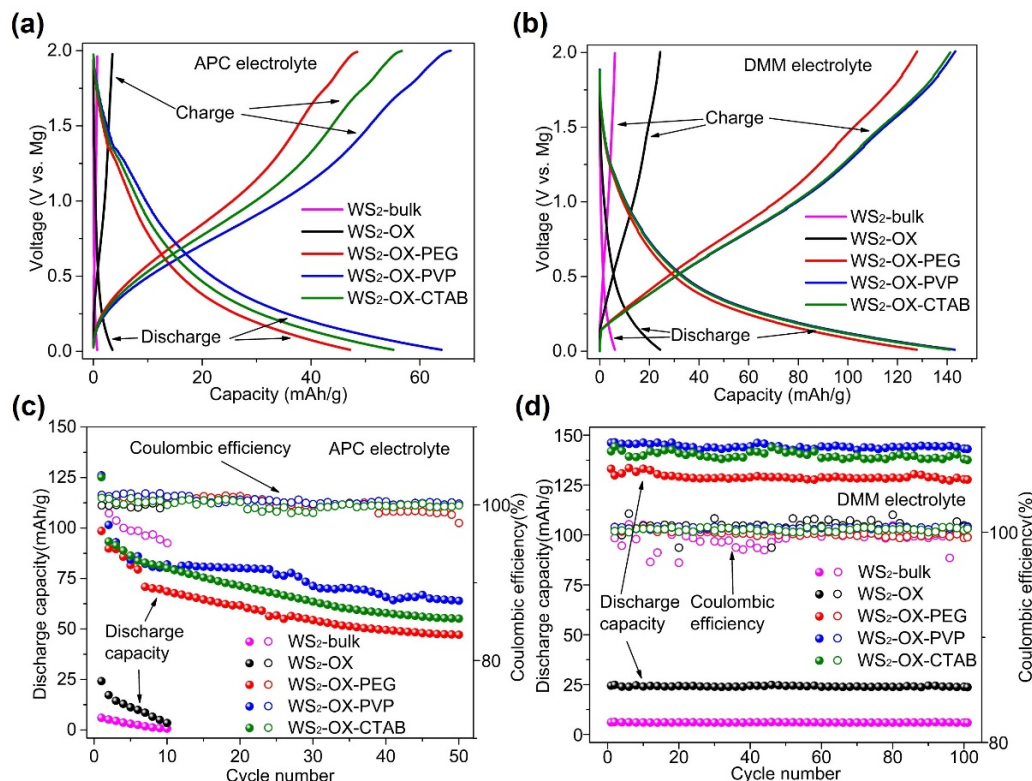
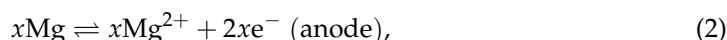


**Figure 3.** The discharge–charge profiles of different morphologies of  $\text{WS}_2$  as magnesium battery cathodes in (a) APC and (b) DMM electrolyte at 500 mA/g after 100th cycle. (c,d) The cycling performance of different morphologies of  $\text{WS}_2$  as magnesium battery cathodes in (c) APC and (d) DMM at 500 mA/g.

The capacity of  $\text{WS}_2$  to host  $\text{Mg}^{2+}$  ions during discharging is given by  $x$  in Equation (1) and is associated with the release of two electrons, as shown by Equation (2).



The theoretical capacity  $C_{theor}$  is calculated according to Equation (3).

$$C_{theor} = N_A e \frac{x n_e}{M_C}, \quad (3)$$

where  $N_A$  is Avogadro's number,  $e$  is the elementary charge,  $n_e$  is the number of electrons needed, i.e., 2, for the oxidation of magnesium to  $\text{Mg}^{2+}$ ,  $M_C$  is the molar mass of the cathode material, which for tungsten sulfide is 247.98 g/mol, and  $x$  as in Equation (1), is the number of ions hosted per formula unit of the cathode (i.e., mols  $\text{Mg}^{2+}$  intercalated per mol of  $\text{WS}_2$ ). The highest observed discharge capacity found for materials in this work was 146.4 mAh/g for  $\text{WS}_2$ -OX-PVP cathode, which substituting in Equation (3) implies

that our  $\text{WS}_2$  cathode was able to host a minimum of 0.68 mol of  $\text{Mg}^{2+}$  ions per formula unit of  $\text{WS}_2$ . In reality, the intercalated quantity is likely to be larger due to polarization and ohmic losses. This intercalated amount of  $\text{Mg}^{2+}$  in  $\text{WS}_2$  is close to that reported for the  $\text{MoS}_2$  cathode ( $\text{Mg}_x\text{MoS}_2$ ,  $x = 0.67$ ) [19].

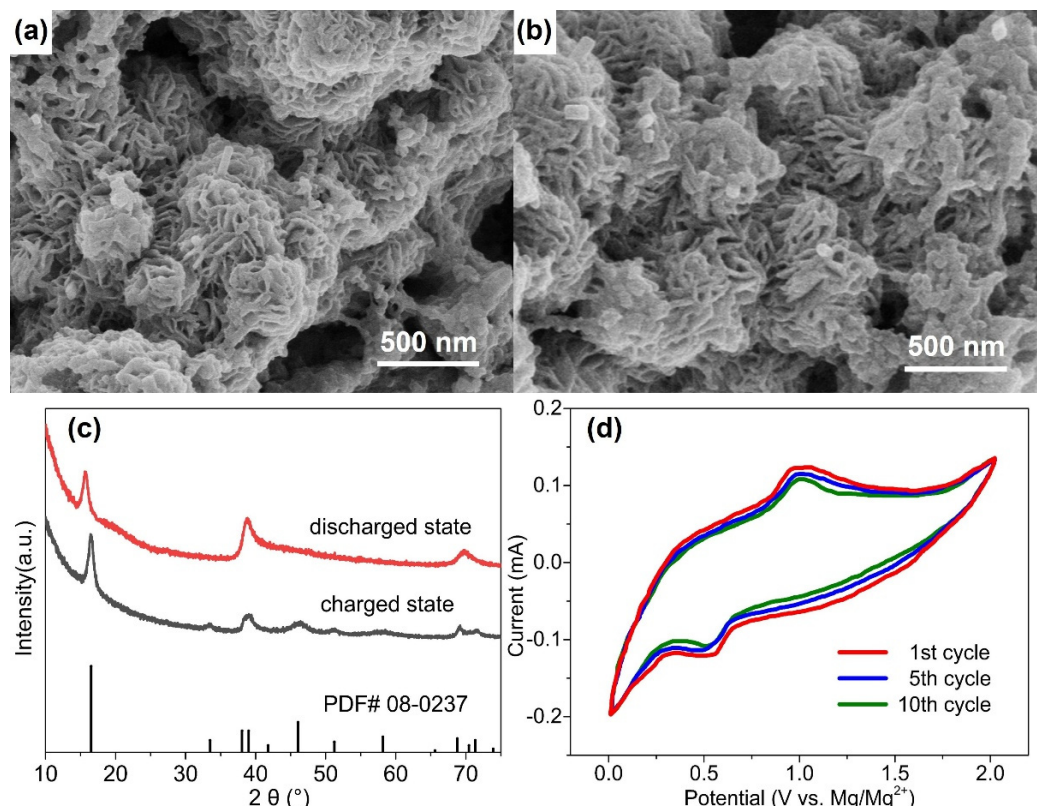


**Figure 4.** SEM micrographs of  $\text{WS}_2$  electrode ( $\text{WS}_2$ -OX-PVP) in DMM electrolyte before the 1st cycle at charged state (a) and after the 100 cycle at discharged state (b); the corresponding XRD patterns are shown in (c); cyclic voltammetry of  $\text{WS}_2$ -OX-PVP at a scan rate of 1 mV/s in DMM electrolyte in the potential window of 0–2 V is shown in (d).

Theoretical first principles studies into magnesium intercalation using density functional theory have indicated that values as high as  $x = 2$  might be achievable. However, the ability of density-functional-theory (DFT) methods to accurately quantify battery material performance is questionable, and such high levels of intercalation have not yet been experimentally observed [45]. Experimental results for cathodes based on  $\text{WS}_2$  have generally achieved lower specific capacities compared to the performance we have observed for the nanostructures reported here, as discussed below. An intercalation capacity at a level of  $x = 0.28$  was reportedly achieved in  $\text{WS}_2$  in an earlier study [23]; however, no conclusive limiting intercalation capacity has been determined for this cathode material.

For the cathode materials examined here, the highest discharge capacities we achieved using a DMM electrolyte are 146.4 mAh/g and 144.3 mAh/g for  $\text{WS}_2$ -OX-PVP and  $\text{WS}_2$ -OX-CTAB cathodes, respectively. In APC, solution capacities for these materials were lower, 126.1 mAh/g ( $\text{WS}_2$ -OX-PVP) and 125.2 mAh/g ( $\text{WS}_2$ -OX-CTAB), illustrating the role of electrolyte/cathode compatibility. The highest discharge capacities of  $\text{WS}_2$ -OX-PVP and  $\text{WS}_2$ -OX-CTAB in DMM correspond to a minimal level of intercalation of approximately 0.68 mol  $\text{Mg}^{2+}$  per mol  $\text{WS}_2$  producing  $\text{Mg}_{\sim 0.68}\text{WS}_2$ . Table S3 presents a summary of reported performance data from previous studies into  $\text{WS}_2$  and other metal sulfide cathode materials in magnesium batteries [17–20,23,46–54]. Figure 5 is drawn to compare this work with the publications mentioned above in the dimension of power density and energy density. From Table S3, the performance we observed in this study for  $\text{WS}_2$  in terms of

the highest achieved capacity lies inside the range of capacities observed for other sulfide materials. However, compared with other materials, this work shows better stable cycling performance and less capacity loss during cycling even under higher current density (Table S3). Furthermore, in consideration of power density and energy density, this work shows the best performance among others (Figure 5), implying possible applications in the field of electric vehicles. Cathodes based on CuS and TiS<sub>2</sub> often rely on conversion reactions between Mg and Cu/Ti and, therefore, generally do not show the kind of stable cycling performance shown here. The capacities of WS<sub>2</sub> cathodes fabricated here were significantly higher than those reported in earlier studies into exfoliated WS<sub>2</sub> and WS<sub>2</sub>-graphene composites as Mg battery cathodes [23]. This demonstrates the efficacy of templating and nanostructuring in conjunction with optimized electrolyte selection. The nanostructured WS<sub>2</sub> cathodes used here with DMM electrolyte present very good reversibility/cyclability and rapid kinetics, showing little capacity decline between 1st and 100th cycles even under a high current density of 500 mA/g. When one considers the cycling stability and initial/final capacities, the materials we studied here compare quite favorably with prior reported studies into analogous sulfide materials. The outstanding performance of our WS<sub>2</sub> cathodes can be related to the unique morphology and microstructure, high specific surface area of WS<sub>2</sub>, good electrochemical properties of electrolytes, fast electron transfer, and insertion/extraction of Mg<sup>2+</sup> ions, as discussed extensively below.

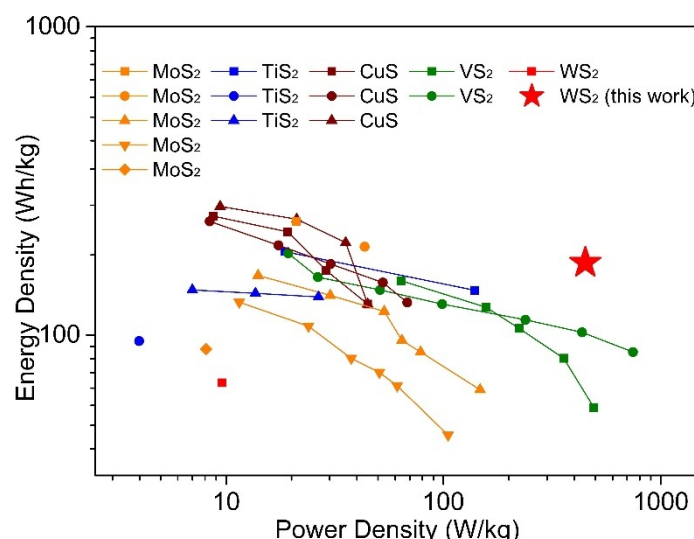


**Figure 5.** Ragone plots for magnesium batteries with different cathodes (by cathode mass). The data about WS<sub>2</sub> and other metal sulfide cathode materials for magnesium batteries are taken from previous studies reported in the references [17–20,23,46–54].

Cathode performance with DMM electrolyte was markedly improved relative to APC electrolyte. The significant diminishment of discharge capacities in cells using APC electrolytes is likely to be attributed to the corrosion of battery components, including current collectors by the halogen in APC. In the APC electrolyte, PhMgCl is the only magnesium salt in the electrolyte, and the halogen comes from both PhMgCl and AlCl<sub>3</sub>. The amount of halogen (Cl) from PhMgCl and AlCl<sub>3</sub> in APC (2 mol/L) is much higher than that in DMM (0.25 mol/L), in which MgTFSI<sub>2</sub> is the major magnesium salt, and MgCl<sub>2</sub> only exists in a small amount. The improved battery performance achieved using DMM as the electrolyte can be attributed to the following facts. In the DMM solution, MgTFSI<sub>2</sub> is not corrosive and is the only magnesium salt soluble in ether leading to good fluidity inside the battery [5]. Further, the small amount of MgCl<sub>2</sub> not only provides an Mg<sup>2+</sup> source but also scavenges residual water under the appropriate voltage range [11].

Clearly, the electrochemical performance of cathodes in this research is affected by the nanostructure morphology that influences the specific surface area and the available

void space between the neighboring nanosheets. Morphologies were controlled by means of sodium oxalate and templating agents, which resulted in profound changes to the formation and structure of tungsten sulfide materials. A closer examination of the formation and templating mechanisms that take place in the processes applied here is presented in the supplementary information. Templating agents, which contain hydrophobic and hydrophilic components, alter the surface energy of solid reactants and products and thus modify the habit of crystal growth in materials. Upon examining the performance of the different cathodes, it is evident that the templated nanostructured WS<sub>2</sub> materials exhibited notably higher performance in terms of capacity and discharge voltage relative to non-templated nanostructured WS<sub>2</sub> and bulk WS<sub>2</sub>. From inspection of the data in Figure 3 and Table S3, the capacity of templated nano WS<sub>2</sub> is much better than that of non-templated WS<sub>2</sub>, with nanoflower WS<sub>2</sub> (WS<sub>2</sub>-OX-PVP and WS<sub>2</sub>-OX-CTAB) showing a clearly higher storage capacity than that of nanorod WS<sub>2</sub> (WS<sub>2</sub>-OX-PEG). The higher surface areas of nanoflower spheres, as confirmed by BET analysis, result in greater levels of surface localized magnesium intercalation and thus correspond as postulated to higher levels of reversible capacity for these materials, as shown in Figure 3 and Table S3. The strength of W-S bonds and interlayer Van der Waals forces affect Mg<sup>2+</sup> mobility and intercalation, which are important in governing the performance of magnesium ion batteries [25,26]. According to the XPS and BET results, both W-S bonds and Van der Waals forces of nanostructured materials are weaker than those of bulk WS<sub>2</sub>, which indicates the layered nanostructure impacts the electrostatic forces between Mg<sup>2+</sup> and cathode hosts and increases the ion mobility and intercalation capacity. Additionally, the templated nanostructured WS<sub>2</sub> shows a higher surface and more defect sites. The difference in results between nanoflower WS<sub>2</sub> and nanorod WS<sub>2</sub> can be attributed to the substantial difference in the specific area and binding energy. The small results difference between forms of nanoflower WS<sub>2</sub> could be attributed to the more uniform surface morphology of nanoflower-sphere WS<sub>2</sub> in the WS<sub>2</sub>-OX-PVP sample.

As the XRD measurement revealed a homogenous WS<sub>2</sub> phase for all samples, a uniform intercalation capability is expected in all materials, and so, neglecting microstructure, the theoretical capacity may be assumed to be constant for all samples. In order to elucidate the morphological origin of the different measured capacities for the materials studied in this work, further electrochemical tests on the cells were conducted (Figure 6). Cells were discharged and then charged in a stepwise manner with pausing intervals of 2 h each used to relax the cell and allow approximation of open circuit voltages (OCV). Following relaxation, EIS measurements were recorded (circles in Figure 6a). Although the relaxation process is not able to reach full equilibrium in only two hours, in the following, the measured potential after the 2 h pause interval is considered as a “pseudo OCV”. The overpotential of a cell is an important indicator of the efficacy of kinetic processes in the cell. We expect higher overpotential values to arise in cases where diffusion pathways are longer and interfacial polarization barriers pose a bottleneck for ion intercalation and release. In Figure 6, the overpotential can be seen as the difference between the half-cell potential prior to and following relaxation. The high overpotential of WS<sub>2</sub>-bulk is expected based on microstructure and cell performance data and is indicative of the longer diffusion pathways and lower levels of the surface area resulting in high interface polarization and more sluggish reactions at interfaces.

Plotting the potential vs. the specific capacity (Figure 6b) reveals relationships between specific capacities and the overpotentials and the pseudo OCVs (dash/dot line in Figure 6b). WS<sub>2</sub>-bulk shows a lower specific capacity and a higher overpotential during relaxation compared to WS<sub>2</sub>-OX-PVP. The pseudo OCV curves from the two WS<sub>2</sub>-OX-PVP samples are rather similar. The higher overpotential of WS<sub>2</sub>-OX-PVP APC leads to a lower specific capacity. The WS<sub>2</sub>-bulk sample shows higher OCV during charging and a lower one while discharging. Whether this behavior is driven by structural factors in the cathode material or by altered relaxation kinetics in the overall system requires further analysis. However, the decreased capacities seen for WS<sub>2</sub>-bulk DMM and WS<sub>2</sub>-OX-PVP APC can be attributed

to the higher overpotentials in these samples, which results in the cutoff voltage of 2 V being reached at an earlier stage with a lower capacity.

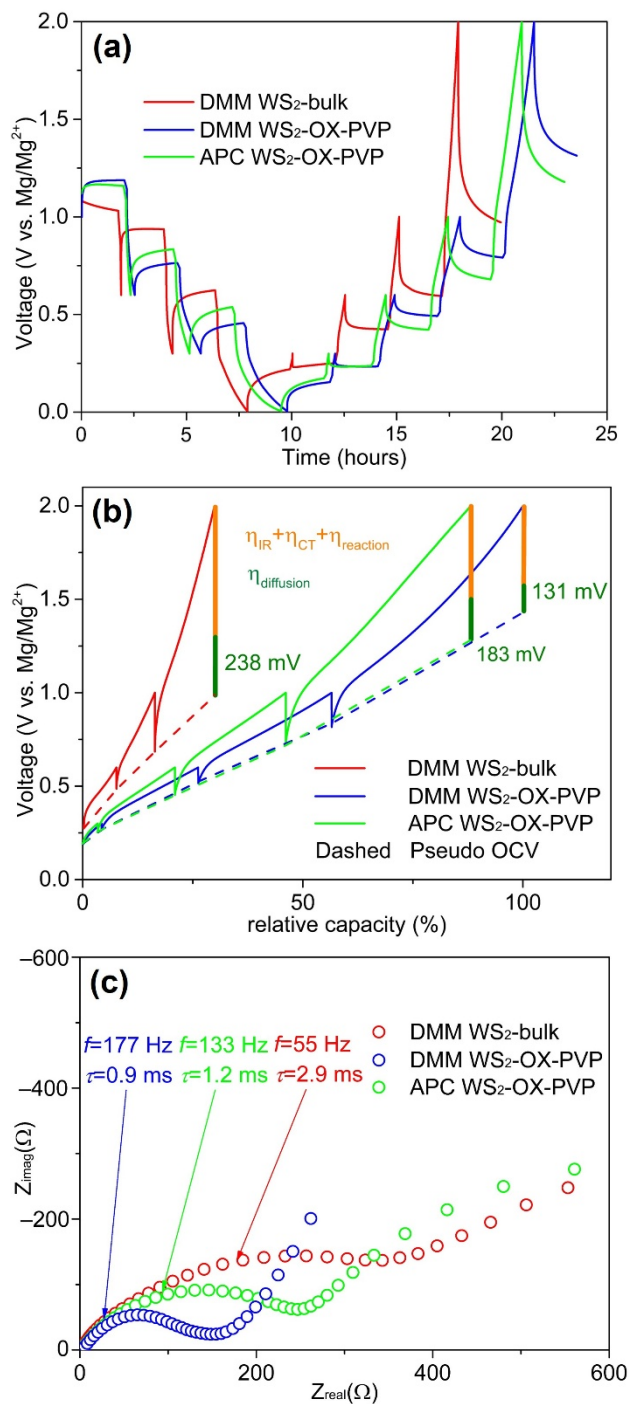


**Figure 6.** (a) Pulsed discharge–charge cycle with 2 h of relaxation at several cell potentials. The circles mark conducted impedance measurements, red circles: measurements discussed here. (b) The same cycle plotted vs. specific capacity. The connected end potentials of the relaxation steps approximate the pseudo OCV curves (dashed lines). (c) Impedance spectra of WS<sub>2</sub>-bulk DMM (red), WS<sub>2</sub>-OX-PVP DMM (blue), and WS<sub>2</sub>-OX-PVP APC (green) after pausing discharge at 0.3 V for 2 h.

From impedance spectra, we can distinguish the individual –contributions of the electrolyte resistance  $R_i$  and the charge transfer resistance  $R_{CT}$ . In Figure 6c, selected EIS spectra are plotted. In Table 1, we list the  $R_i$ ,  $R_{CT}$ , and  $R_{(f=50mHz)}$  (at the measured

frequency of 50 mHz) and the relaxation time constant of the charge transfer process  $\tau_{CT} = 1/(2\pi f_{max})$  from these EIS spectra.  $R_i$  is constant at approx. 2  $\Omega$  for all samples and all EIS measurements, indicating a consistent electrolyte conductivity, regardless of whether DMM or APC was used. However, these values are very low compared to the  $R_{CT}$  and  $R_{(f=50mHz)}$  values.  $R_{CT}$  is lowest for WS<sub>2</sub>-OX-PVP DMM and highest for WS<sub>2</sub>-bulk DMM. The same trend is observable for  $R_{(f=50mHz)}$ .  $R_{CT}$  and  $\tau_{CT}$  can be linked to the high surface area of the WS<sub>2</sub>-OX-PVP sample (as described earlier), reducing the charge transfer resistance and facilitating the reaction indicated by the lower  $\tau_{CT}$ . The APC electrolyte in the WS<sub>2</sub>-OX-PVP APC sample shows higher resistance values compared to WS<sub>2</sub>-OX-PVP DMM. Furthermore, from the EIS spectrum, a second distinct process becomes obvious at lower frequencies of ca. 0.2 Hz. Since it is not visible for WS<sub>2</sub>-OX-PVP DMM and WS<sub>2</sub>-bulk DMM, it can also be attributed to the APC electrolyte, deteriorating the performance as shown in the cycling tests above.  $R_{(f=50mHz)}$  arises due through diffusion processes. From these EIS measurements in the frequency domain down to 50 mHz the validity of diffusion processes with their high constants of relaxation times is limited. A better insight into this issue can be derived from the potential drop during relaxation in the time domain. Here the influence of the diffusion process manifested by its overpotential can be investigated. The total voltage drop contains, besides the diffusion overpotential  $\eta_{diffusion}$ , the  $IR_i$  drop and charge transfer reaction overpotential  $\eta_{CT}$  and  $\eta_{reaction}$ , respectively, but they relax immediately and after a few milliseconds (see  $\tau_{CT}$  in Table 1) after setting the charge current to zero. The estimated diffusion overpotentials (Table 1) reveal the same trend as the EIS results, with the lowest values for WS<sub>2</sub>-OX-PVP with DMM electrolyte and the highest for WS<sub>2</sub>-bulk with DMM electrolyte.

**Table 1.** Characteristic parameters from impedance spectra from EIS measurement and the relaxation voltage preceding EIS measurement.

Sample	$R_i$ ( $\Omega$ )	$R_{CT}$ ( $\Omega$ )	$R_{(f=50mHz)}$ ( $\Omega$ )	$\tau_{CT}$ (ms)	$\eta_{diffusion}$ (mV)
method	EIS	EIS	EIS	EIS	Pause before EIS
WS <sub>2</sub> -bulk DMM	2	341	1612	2.9	238
WS <sub>2</sub> -OX-PVP DMM	2	127	266	0.9	131
WS <sub>2</sub> -OX-PVP APC	2	242	894	1.2	183

#### 4. Conclusions

We produced nanostructured WS<sub>2</sub> with different morphologies by means of a hydrothermal method and applied these materials as cathodes in magnesium-ion batteries. The morphologies of nanorods, nanoflower-spheres, and nanoflower-aggregates were acquired by adding Na<sub>2</sub>C<sub>2</sub>O<sub>4</sub> as a complexing agent and adding PEG, PVP, and CTAB as templates. APC and DMM electrolytes were both examined for comparison. Results show that a high capacity of 142.7 mAh/g, which corresponds to 0.68 mol of intercalated Mg<sup>2+</sup> ions per mol of WS<sub>2</sub>, was achieved after 100 cycles at a high current density of 500 mA/g with the flower-like nanostructured WS<sub>2</sub> cathode in DMM electrolyte. The fast Mg<sup>2+</sup> transmission kinetics could be attributed to the smaller molecule size of MgTFSI<sub>2</sub>/MgCl<sub>2</sub> compared with that of PhMgCl/AlCl<sub>3</sub>, weaker ionic bonds, and van der Waals forces of WS<sub>2</sub> compared with other transition metal oxides/sulfides and increased surface area after nanostructurization.

**Supplementary Materials:** The following supporting information can be downloaded at <https://www.mdpi.com/article/10.3390/batteries8090116/s1>; Figure S1: Le Bail fit of XRD patterns of WS<sub>2</sub>-bulk sample using a model for (a) isotropic size and (b) anisotropic size broadening; Figure S2: Schematic description of magnesium ion intercalation in WS<sub>2</sub> cathode; Table S1: A summary of structural parameters extracted by Le Bail fitting of powder XRD patterns of samples WS<sub>2</sub>-bulk, WS<sub>2</sub>-OX, WS<sub>2</sub>-OX-PEG, WS<sub>2</sub>-OX-PVP and WS<sub>2</sub>-OX-CTAB; Table S2: Peak energy, peak width, peak area and

Lorentzian/Gaussian (L/G) ratios of different WS<sub>2</sub> samples; Table S3: Summary of reported cycling stability for metal sulfides as cathodes in magnesium batteries.

**Author Contributions:** W.G.: Conceptualization, Methodology, Investigation, Data Curation, Writing—Original Draft. D.A.H.H.: Conceptualization, Writing—Review and Editing, Supervision, Project administration. D.K.: Methodology, Investigation, Data Curation, Writing—Review and Editing. J.W.: Investigation, Data Curation, M.F.B.: Conceptualization, Investigation, Data Curation, Writing—Review and Editing, Supervision, Project administration, A.G.: Conceptualization, Supervision, Writing—Review and Editing, Resources. All authors have read and agreed to the published version of the manuscript.

**Funding:** This research was funded by China Scholarship Council (201606280048).

**Institutional Review Board Statement:** Not applicable.

**Informed Consent Statement:** Not applicable.

**Data Availability Statement:** The data that support the findings of this study are available from the corresponding author upon reasonable request.

**Acknowledgments:** Wuqi Guo acknowledges the financial support from the China Scholarship Council. The authors acknowledge support from the German Research Foundation and the Open Access Publication Fund of TU Berlin.

**Conflicts of Interest:** The authors declare no conflict of interest.

## References

- Shao, G.; Hanaor, D.A.H.; Wang, J.; Kober, D.; Li, S.; Wang, X.; Shen, X.; Bekheet, M.F.; Gurlo, A. Polymer-Derived SiOC Integrated with a Graphene Aerogel As a Highly Stable Li-Ion Battery Anode. *ACS Appl. Mater. Inter.* **2020**, *12*, 46045–46056. [[CrossRef](#)] [[PubMed](#)]
- Wang, J.; Kober, D.; Shao, G.; Epping, J.D.; Görke, O.; Li, S.; Gurlo, A.; Bekheet, M.F. Stable anodes for lithium-ion batteries based on tin-containing silicon oxycarbonitride ceramic nanocomposites. *Mater. Today Energy* **2022**, *26*, 100989. [[CrossRef](#)]
- Su, Y.-S.; Hsiao, K.-C.; Sireesha, P.; Huang, J.-Y. Lithium Silicates in Anode Materials for Li-Ion and Li Metal Batteries. *Batteries* **2022**, *8*, 2. [[CrossRef](#)]
- Houache, M.S.E.; Yim, C.-H.; Karkar, Z.; Abu-Lebdeh, Y. On the Current and Future Outlook of Battery Chemistries for Electric Vehicles Mini Review. *Batteries* **2022**, *8*, 70. [[CrossRef](#)]
- Muldoon, J.; Bucur, C.B.; Gregory, T. Fervent Hype behind Magnesium Batteries: An Open Call to Synthetic Chemists-Electrolytes and Cathodes Needed. *Angew. Chem. -Int. Ed.* **2017**, *56*, 12064–12084. [[CrossRef](#)]
- Ponrouch, A.; Bitenc, J.; Dominko, R.; Lindahl, N.; Johansson, P.; Palacin, M.R. Multivalent rechargeable batteries. *Energy Storage Mater.* **2019**, *20*, 253–262. [[CrossRef](#)]
- Bucur, C.B.; Gregory, T.; Oliver, A.G.; Muldoon, J. Confession of a Magnesium Battery. *J. Phys. Chem. Lett.* **2015**, *6*, 3578–3591. [[CrossRef](#)]
- Gautam, G.S.; Hannah, D.C.; Malik, R.; Liu, M.; Canepa, P.; Sai Gautam, G.; Gallagher, K.G.; Persson, K.A.; Ceder, G. Odyssey of Multivalent Cathode Materials: Open Questions and Future Challenges. *Chem. Rev.* **2017**, *117*, 4287–4341. [[CrossRef](#)]
- Aurbach, D.; Choi, J.W. Promise and reality of post-lithium-ion batteries with high energy densities. *Nat. Rev. Mater.* **2016**, *1*, 16013. [[CrossRef](#)]
- Zeng, W.; Li, Y.; Kuang, C. A Review of Electrode for Rechargeable Magnesium Ion Batteries. *J. Nanosci. Nanotechnol.* **2019**, *19*, 12–25. [[CrossRef](#)]
- Bucur, C.B.; Gregory, T.; Muldoon, J. Quest for Nonaqueous Multivalent Secondary Batteries: Magnesium and Beyond. *Chem. Rev.* **2014**, *114*, 11683–11720. [[CrossRef](#)]
- Lu, Z.; Schechter, A.; Gofer, Y.; Gizbar, H.; Aurbach, D.; Turgeman, R.; Cohen, Y.; Moshkovich, M.; Levi, E. Prototype systems for rechargeable magnesium batteries. *Nature* **2000**, *407*, 724–727. [[CrossRef](#)]
- Xu, J.; Wei, Z.; Liu, H.; Li, Y.; Mei, L.; Ma, J.; Dou, S. Chevrel Phase Mo<sub>6</sub>T<sub>8</sub>(T=S, Se) as Electrodes for Advanced Energy Storage. *Small* **2017**, *13*, 1701441. [[CrossRef](#)]
- Bonnick, P.; Nazar, L.F.; Sun, X. Layered TiS<sub>2</sub> Positive Electrode for Mg Batteries. *Acs Energy Lett.* **2016**, *1*, 297–301. [[CrossRef](#)]
- Chou, C.-Y.; Yang, C.-H.; Lee, T.-C.; Chang, J.-K.; Hsu, C.-J. MoS<sub>2</sub>/graphene cathodes for reversibly storing Mg<sup>2+</sup> and Mg<sup>2+</sup>/Li<sup>+</sup> in rechargeable magnesium-anode batteries. *Chem. Commun.* **2016**, *52*, 1701–1704. [[CrossRef](#)]
- Devaraju, M.K.; Nakayasu, Y.; Tamura, N.; Sasaki, Y.; Truong, Q.D.; Kempaiah Devaraju, M.; Tomai, T.; Honma, I. Exfoliated MoS<sub>2</sub> and MoSe<sub>2</sub> Nanosheets by a Supercritical Fluid Process for a Hybrid Mg-Li-Ion Battery. *Acs Omega* **2017**, *2*, 2360–2367. [[CrossRef](#)]
- Fan, L.-Z.; Jiao, L.; Liu, Y. Graphene intercalated in graphene-like MoS<sub>2</sub>: A promising cathode for rechargeable Mg batteries. *J. Power Source* **2017**, *340*, 104–110. [[CrossRef](#)]

18. Liang, Y.; Feng, R.; Yang, S.; Ma, H.; Liang, J.; Chen, J. Rechargeable Mg Batteries with Graphene-like MoS<sub>2</sub> Cathode and Ultrasmall Mg Nanoparticle Anode. *Adv. Mater.* **2011**, *23*, 640–643. [[CrossRef](#)]
19. Jiao, L.; Wu, Q.; Du, J.; Zhao, Y.; Liu, Y.; Si, Y.; Wang, Y.; Yuan, H. Sandwich-structured graphene-like MoS<sub>2</sub>/C microspheres for rechargeable Mg batteries. *J. Mater. Chem. A* **2013**, *1*, 5822–5826. [[CrossRef](#)]
20. Liang, Y.; Dong, H.; Lin, J.; Wang, H.; Yoo, H.D.; Liu, Y.; Ma, L.; Wu, T.; Li, Y.; Ru, Q.; et al. Fast kinetics of magnesium monochloride cations in interlayer-expanded titanium disulfide for magnesium rechargeable batteries. *Nat. Commun.* **2017**, *8*, 339. [[CrossRef](#)]
21. Shi, L.; Zhang, Y.; Liu, Z.; Chen, K. Scalable chemical-vapour-deposition growth of three-dimensional graphene materials towards energy-related applications. *Chem. Soc. Rev.* **2018**, *47*, 3018–3036. [[CrossRef](#)]
22. Zhou, F.; Huang, Z.-H.; Yao, W.-T.; Zhang, T.-W.; Tan, Y.-H.; Yao, H.-B.; Lu, L.-L.; Yu, S.-H. MoS<sub>2</sub>-Nanosheet-Decorated Carbon Nanofiber Composites Enable High-Performance Cathode Materials for Mg Batteries. *Chemelectrochem* **2018**, *5*, 996–1001. [[CrossRef](#)]
23. Biswas, S.; Rani, J.V.; Latha, M. Application of WS<sub>2</sub>-G composite as cathode for rechargeable magnesium batteries. *Ionics* **2020**, *26*, 3395–3404. [[CrossRef](#)]
24. Regulacio, M.D.; Nguyen, D.T.; Horia, R.; Seh, Z.W. Designing Nanostructured Metal Chalcogenides as Cathode Materials for Rechargeable Magnesium Batteries. *Small* **2021**, *17*, 2007683. [[CrossRef](#)]
25. Wei, Z.; Liao, J.; Ni, W.; Wang, C.; Huang, J.; Ma, J. Molybdenum and tungsten chalcogenides for lithium/sodium-ion batteries: Beyond MoS<sub>2</sub>. *J. Energy Chem.* **2019**, *33*, 100–124. [[CrossRef](#)]
26. Yu, X.; Zhang, L.; Zhou, F.; Liang, Y.; Zhang, X.; Wang, R. Molybdenum Phosphide/Carbon Nanotube Hybrids as pH-Universal Electrocatalysts for Hydrogen Evolution Reaction. *Adv. Funct. Mater.* **2018**, *28*, 1706523. [[CrossRef](#)]
27. Salama, M.; Yoo, H.D.; Gofer, Y.; Park, J.-B.; Shterenberg, I.; Sun, Y.-K.; Aurbach, D. Evaluation of (CF<sub>3</sub>SO<sub>2</sub>)<sub>2</sub>N<sup>−</sup> (TFSI) Based Electrolyte Solutions for Mg Batteries. *J. Electrochem. Soc.* **2015**, *162*, A7118–A7128. [[CrossRef](#)]
28. Chen, W.; Huang, J.; Yan, C.; Sun, H.; Lei, T.; Wang, C.; Zhang, W.; Li, Y.; Xiong, J. Multi-Functional Layered WS<sub>2</sub> Nanosheets for Enhancing the Performance of Lithium-Sulfur Batteries. *Adv. Energy Mater.* **2017**, *7*, 1601843. [[CrossRef](#)]
29. David, L.; Singh, G.; Bhandavat, R. Synthesis of Surface-Functionalized WS<sub>2</sub> Nanosheets and Performance as Li-Ion Battery Anodes. *J. Phys. Chem. Lett.* **2012**, *3*, 1523–1530. [[CrossRef](#)]
30. Dou, S.; Wang, G.; Su, D. WS<sub>2</sub>@graphene nanocomposites as anode materials for Na-ion batteries with enhanced electrochemical performances. *Chem. Commun.* **2014**, *50*, 4192–4195. [[CrossRef](#)]
31. Liao, J.; Chen, C.; Yang, J.; Chen, J.; Song, Y.; Gong, F.; Wang, S.; Xu, Z.; Wu, M. Controllable morphologies and electrochemical performances of self-assembled nano-honeycomb WS<sub>2</sub> anodes modified by graphene doping for lithium and sodium ion batteries. *Carbon* **2019**, *142*, 697–706. [[CrossRef](#)]
32. Padya, B.; Venkatesh, L.; Chakravadhanula, V.S.K.; Pandey, A.K.; Adigilli, H.K.; Joardar, J. Oxidation of 2D-WS<sub>2</sub> nanosheets for generation of 2D-WS<sub>2</sub>/WO<sub>3</sub> heterostructure and 2D and nanospherical WO<sub>3</sub>. *Phys. Chem. Chem. Phys.* **2019**, *21*, 25139–25147. [[CrossRef](#)]
33. Kyotani, T.; Tomita, A.; Sharma, A.; Kyotani, T.; Tomita, A. Comparison of structural parameters of PF carbon from XRD and HRTEM techniques. *Carbon* **2000**, *38*, 1977–1984. [[CrossRef](#)]
34. Le Bail, A. Whole powder pattern decomposition methods and applications: A retrospection. *Powder Diffr.* **2005**, *20*, 316–326. [[CrossRef](#)]
35. Rodriguez-Carvajal, J. Recent developments of the program FULLPROF, commission on powder diffraction. *IUCr Newsl.* **2001**, *26*, 12–19.
36. Finger, L.W.; Cox, D.E.; Jephcoat, A.P. A correction for powder diffraction peak asymmetry due to axial divergence. *J. Appl. Crystallogr.* **1994**, *27*, 892–900. [[CrossRef](#)]
37. Diesner, K.; Fiechter, S.; Moser, J.H.; Levy, F.; Ennaoui, A.; Lévy, F. Structural analysis of 2H-WS<sub>2</sub> thin films by X-ray and TEM investigation. *Thin Solid Films* **1997**, *311*, 146–150. [[CrossRef](#)]
38. Jha, R.; Guha, P. An effective liquid-phase exfoliation approach to fabricate tungsten disulfide into ultrathin two-dimensional semiconducting nanosheets. *J. Mater. Sci.* **2017**, *52*, 7256–7268. [[CrossRef](#)]
39. Wang, Y.; Roller, J.; Maric, R. Morphology-Controlled One-Step Synthesis of Nanostructured LiNi<sub>1/3</sub>Mn<sub>1/3</sub>Co<sub>1/3</sub>O<sub>2</sub> Electrodes for Li-Ion Batteries. *ACS Omega* **2018**, *3*, 3966–3973. [[CrossRef](#)]
40. Attias, R.; Hirsch, B.; Yemini, R.; Gofer, Y.; Salama, M.; Noked, M.; Aurbach, D. On the Feasibility of Practical Mg–S Batteries: Practical Limitations Associated with Metallic Magnesium Anodes. *ACS Appl. Mater. Interfaces* **2018**, *10*, 36910–36917. [[CrossRef](#)]
41. Dong, S.; Cui, Z.; Du, A.; Li, G.; Zhang, Z.; Cui, G. Rechargeable Magnesium Batteries using Conversion-Type Cathodes: A Perspective and Minireview. *Small Methods* **2018**, *2*, 1800020. [[CrossRef](#)]
42. Choi, S.H.; Boo, S.J.; Lee, J.-H.; Kang, Y.C. Electrochemical properties of tungsten sulfide–carbon composite microspheres prepared by spray pyrolysis. *Sci. Rep.* **2014**, *4*, 5755. [[CrossRef](#)] [[PubMed](#)]
43. Zhang, R.; Bao, J.; Pan, Y.; Sun, C.-F. Highly reversible potassium-ion intercalation in tungsten disulfide. *Chem. Sci.* **2019**, *10*, 2604–2612. [[CrossRef](#)]
44. Wu, Y.; Xu, Y.; Li, Y.; Lyu, P.; Wen, J.; Zhang, C.; Zhou, M.; Fang, Y.; Zhao, H.; Kaiser, U.; et al. Unexpected intercalation-dominated potassium storage in WS<sub>2</sub> as a potassium-ion battery anode. *Nano Res.* **2019**, *12*, 2997–3002. [[CrossRef](#)]

45. Gujarathi, A.M.; Al Rawahi, N.; Mohammadi, M.; Vakili-Nezhaad, G.R. Performance of WS<sub>2</sub> monolayers as a new family of anode materials for metal-ion (Mg, Al and Ca) batteries. *Mater. Chem. Phys.* **2019**, *230*, 114–121. [[CrossRef](#)]
46. Wang, D.; Di, Y.; Wei, L.; Liu, B.; Zhao, Y.; Wang, X.; Chen, G.; Wei, Y. Superior Mg<sup>2+</sup> storage properties of VS<sub>2</sub> nanosheets by using an APC-PP<sub>14</sub>Cl/THF electrolyte. *Energy Storage Mater.* **2019**, *23*, 749–756. [[CrossRef](#)]
47. Chen, R.; Yan, C.; Zhao, P.; Hu, Y.; Xue, X.; Kong, W.; Lin, H.; Wang, L.; Jin, Z. One-Step Synthesis of 2-Ethylhexylamine Pillared Vanadium Disulfide Nanoflowers with Ultralarge Interlayer Spacing for High-Performance Magnesium Storage. *Adv. Energy Mater.* **2019**, *9*, 1900145. [[CrossRef](#)]
48. Du, C.L.; Zhu, Y.Q.; Wang, Z.T.; Wang, L.Q.; Younas, W.; Ma, X.L.; Cao, C.B. Cuprous Self-Doping Regulated Mesoporous CuS Nanotube Cathode Materials for Rechargeable Magnesium Batteries. *Acs Appl. Mater. Interfaces* **2020**, *12*, 35035–35042. [[CrossRef](#)]
49. Wang, Z.; Zhu, Y.; Peng, H.; Du, C.; Ma, X.; Cao, C. Microwave-induced phase engineering of copper sulfide nanosheets for rechargeable magnesium batteries. *Electrochim. Acta* **2021**, *374*, 137965. [[CrossRef](#)]
50. Huang, J.; Zhu, Y.; Du, C.; Han, Z.; Yao, X.; Yang, X.; Cao, Y.; Zhang, Y.; Ma, X.; Cao, C. Hierarchical nanosheet-assembled copper sulfide microspheres as the cathode materials for rechargeable magnesium batteries. *Electrochim. Acta* **2021**, *388*, 138619. [[CrossRef](#)]
51. Bonnick, P.; Duffort, V.; Liu, M.; Rong, Z.; Sun, X.; Persson, K.A.; Ceder, G.; Nazar, L.F. A high capacity thiospinel cathode for Mg batteries. *Energy Environ. Sci.* **2016**, *9*, 2273–2277. [[CrossRef](#)]
52. Guan, X.; Lv, R.; Wang, D.; Liu, P.; Zhang, J.; Luo, J. Rechargeable Mg metal batteries enabled by a protection layer formed in vivo. *Energy Storage Mater.* **2020**, *26*, 408–413. [[CrossRef](#)]
53. Wu, C.; Zhao, G.; Yu, X.; Liu, C.; Lyu, P.; Maurin, G.; Le, S.; Sun, K.; Zhang, N. MoS<sub>2</sub>/graphene heterostructure with facilitated Mg-diffusion kinetics for high-performance rechargeable magnesium batteries. *Chem. Eng. J.* **2021**, *412*, 128736. [[CrossRef](#)]
54. Wu, C.L.; Zhang, L.; Zhao, G.Y.; Yu, X.B.; Liu, C.; He, J.J.; Sun, K.N.; Zhang, N.Q. Interlayer-Expanded MoS<sub>2</sub> Containing Structural Water with Enhanced Magnesium Diffusion Kinetics and Durability. *Chemelectrochem* **2021**, *8*, 4559–4563. [[CrossRef](#)]